Available online at www.sciencedirect.com
ScienceDirect
Journal of Sound and Vibration 299 (2007) 1049–1073
JOURNAL OF SOUND AND VIBRATION
www.elsevier.com/locate/jsvi

Dynamic lateral torsional post-buckling of a beam-mass system: Experiments

O. Yogev, I. Bucher, M.B. Rubin*

Faculty of Mechanical Engineering, Technion—Israel Institute of Technology, 32000 Haifa, Israel

Received 9 January 2006; received in revised form 3 August 2006; accepted 9 August 2006
Available online 4 October 2006

Abstract

The phenomenon of static lateral torsional buckling of a beam with a narrow rectangular cross-section is well known. Specifically, a beam is clamped at one of its ends and is subjected to a shear force at its other end which causes deformation in the principal plane with stiffest resistance to bending. Above a critical value of load, a bifurcation occurs and the beam twists and experiences out-of-plane deformation which tends to transfer bending to the plane of weakest resistance. Here, attention is focused on an experimental study of dynamic lateral torsional buckling. In the experiment, a beam is attached to the shaft of a motor at one of its ends and a relatively large mass is attached to its other end. Rotation of the motor causes deflection of the beam in its principal plane of stiffest bending resistance. By increasing the excitation frequency and/or amplitude of oscillation of the motor's shaft, the shear force applied by the mass on the beam's end exceeds a critical value which causes dynamic lateral torsional buckling of the beam. Special techniques have been developed to produce and measure this phenomenon and the data has been presented in a form that can be used for future validation of analytical or numerical models.

1. Introduction

Lateral torsional buckling of a cantilever beam subjected to a shear force is a well-known phenomena in static stability theory [1, Section 6.3]. Specifically, when the beam has a rectangular cross-section with its height h much greater than its width w, the stiffness to bending is much greater when the shear load is directed in the height direction than when it is directed in the width direction. Furthermore, when the shear load directed in the height direction reaches a critical value, the resistance to torsion is substantially reduced and lateral torsional buckling occurs as the beam twists and deforms out-of-plane with a tendency to transfer bending to the plane of weakest resistance.

Dugundji and Mukhopadhyay [2] studied bending-torsional vibrations of a ribbon. In their experiment the ribbon was free at one of its ends and the other end was clamped to a translational shaker that excited motion oriented in the stiffest cross-sectional bending direction. Their experiment and analysis focused on nearly

*Corresponding author. Tel.: +972 4 829 3188; fax: +972 4 829 5711.
E-mail address: mbrubin@tx.technion.ac.il (M.B. Rubin).

0022-460X/$ - see front matter © 2006 Elsevier Ltd. All rights reserved.
doi:10.1016/j.jsv.2006.08.006

planar vibrations. However, they observed that at large amplitude excitations the beam would experience snap-through-type buckling.

Cusumano and Moon [3] studied chaotic vibrations of a ribbon. In their experiment the ribbon was free at one of its ends and the other end was clamped to a translational shaker that excited motion oriented in the weakest cross-sectional bending direction. Wedge-shaped boundaries near multiples of the natural frequencies of the ribbon where determined within which chaotic response was observed [3, Fig. 5]. Also, a somewhat stable symmetry-breaking steady state period-two subharmonic solution was observed near the third natural frequency.

In the experiments of Dugundji and Mukhopadhyay [2], the length L of the ribbon was not that long relative to its height h ($L/h = 8$) and its height h was very much greater than its width w ($h/w = 150$). Moreover, in the experiments of Cusumano and Moon [3] the length L of the ribbon was long relative to its height h ($L/h = 22.7$) and its height h was very much greater than its width w ($h/w = 127$). In view of this very tall cross-section it is expected that variations in the height direction may influence the response of the ribbon for many modes of vibrations. Consequently, beam theory is not adequate to model the complete response of these plate-like ribbons. In particular, the chaotic response observed by Cusumano and Moon [3] may be influenced by snap-through behavior of the shallow arch in the height direction caused by anticlastic bending due to bending in the weakest cross-sectional bending direction of the ribbon.

In this paper, attention is focused on the design of a beam-mass system which exhibits dynamic lateral torsional post-buckling response. The excitation system is different from that used in either of the experiments by Dugundji and Mukhopadhyay [2] or by Cusumano and Moon [3]. Here, a beam of length L, with rectangular cross-section of height h and width w was clamped at one of its ends to the shaft of a motor, and a rectangular block was clamped at its other end (see Fig. 1). The mass of the block was about 17 times that of the beam. Also, the dimensions of the beam ($L/h = 21.7$; $h/w = 12$) were more consistent with the standard assumption of beam theory (that variations through the cross-section are nearly linear) than those of the ribbons used by Dugundji and Mukhopadhyay [2] or by Cusumano and Moon [3]. Moreover, the rotation of the motor shaft was controlled to be sinusoidal with specified amplitude and frequency and for the in-plane response this rotation caused a shear force to be applied in the orientation of the stiffest cross-sectional bending direction. Despite some similarity with previous works, the different geometrical proportions and boundary conditions, make the phenomena observed in these experiments quite different from those studied by either Dugundji and Mukhopadhyay [2] or Cusumano and Moon [3]. In particular, the beam-mass system was designed in this study so that out-of-plane buckling occurs at frequencies which are distinct from the linear resonance frequencies of the system.

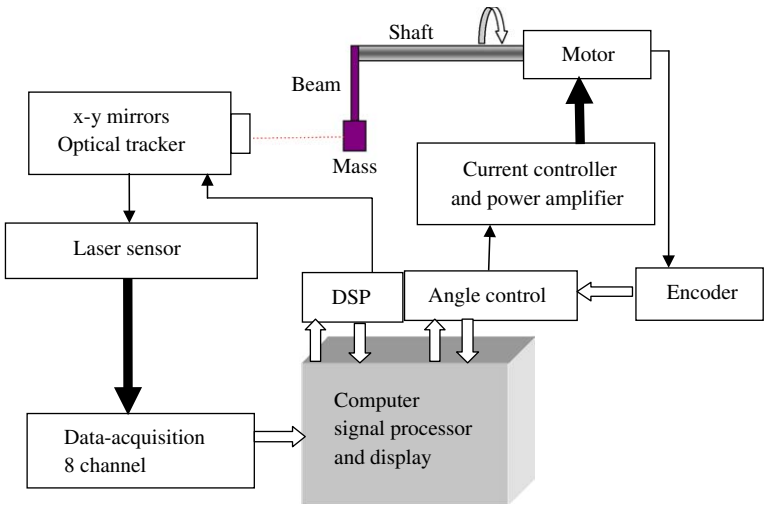

Fig. 1. Schematic of the experimental setup.

Due to the large mass of the block, the dynamically induced shear force can exceed the magnitude for static lateral torsional buckling. For high enough values of this shear force the beam and mass (block) exhibit out-of-plane motion. Two main nonlinear modes of vibration were observed. One mode was characterized by bending in the weakest cross-sectional bending direction coupled with torsion of the block with its center of mass moving out-of-plane. The other mode was characterized by an oscillating rotation of the block with its center of mass remaining relatively fixed and with the beam experiencing mainly second mode bending in its weakest cross-sectional plane with some associated torsion. Both modes were quite stable and relatively periodic. Also, it was observed that these nonlinear deformations occurred when the input forcing amplitude was almost imperceptible. This later observation is similar to that reported by Cusumano and Moon [3, p. 194]. Moreover, such behavior makes this phenomenon hard to control in a closed-loop system.

An outline of this paper is as follows. Section 2 and Appendix A discuss a simple model that was used to design the experimental setup. Since the response of the beam-mass system is nonlinear when buckling occurs it is quite difficult to accurately measure the bending and torsion of the beam. Consequently, a number of non-standard measurement techniques are used to retrieve and to analyze the experimental data. Section 3 discusses the response of the system to a continuously swept-sine wave (CHIRP) loading which was used to identify the natural frequencies of the system and the region of the loading parameters where the buckling phenomena occurs. Section 4 describes an asynchronous, continuous scanning laser sensor procedure for accurately measuring torsion and Section 5 describes image processing edge detection methods for measuring bending and torsion of the beam. Section 6 discusses direct measurements of the natural frequencies of the system and Section 7 shows that gravity has a significant effect on the system. Finally, Section 8 presents conclusions.

2. Design of the experimental setup

The experimental setup is shown schematically in Fig. 1. A beam-mass system is attached to the shaft of a motor which was controlled to oscillate with a sinusoidal rotation angle $\phi(t)$ with amplitude ϕ_0 and frequency ω, such that

$$\phi(t) = \phi_0 \sin(\omega t). \tag{2.1}$$

A cylindrical steel bar of radius 10 mm and length 400 mm was attached to the end of the motor shaft as an extension to allow more freedom of motion for the beam-mass system. This extension bar was supported by two bearings, each of width 20 mm, which were placed at distances 210 and 335 mm from the shaft's end which was clamped to the beam. This extension bar and the bearings introduced some undesirable flexibility and damping to the system which will be discussed later.

An encoder measured the rotation angle of the motor's shaft before its attachment to the extension bar and a laser sensor was used to measure the velocity tangent to the laser beam of points on the mass. In most of the experiments the laser beam was fixed in space. However, in some of the experiments the laser beam was controlled to move in the horizontal plane so that it approximately tracked the motion of the mass, assuming near rigid body motion of the beam-mass system, or so that it scanned different material points in order to separate effects of bending and torsion. For the large deformations and torsion angles that occur during dynamic buckling the laser sensor is not able to track a material point on the mass. Taking into account the band pass of the motor, the sensitivity of the encoder and the characteristics of the controller, the range of amplitude ϕ_0 and frequency ω were limited to

$$0 \leqslant \phi_0 \leqslant 2^\circ, \quad 0 \leqslant \omega \leqslant 50\,\text{Hz}. \tag{2.2}$$

Also, in some of the experiments a high speed video camera capable of taking up to 1000 frames/s was used to obtain a video of the deforming beam-mass system.

The specimen used in these experiments consists of a beam of mass m made from spring steel with a length L, and rectangular cross-section with height h and width w. One end of the beam was clamped to a block of stainless steel which was attached to an extension of the shaft of the motor such that the clamping occurred at a radius $R = 30$ mm from the center of the motor shaft. A steel block of mass M, length B, height H and width W was clamped to the other end of the beam, such that L was the length of the free section between these two

clamped boundaries (see Fig. 2). The clamping system was specially designed to ensure maximum clamping, with the beam being perpendicular to the clamping block and with the mass (block) being properly centered relative to the beam. The clamping screws were countersunk with minimum gap dimensions so that the clamped mass (block) was nearly solid. Also, attempts were made to straighten the beam to minimize perturbations which might cause spurious out-of-plane motion.

The elastic Young's modulus E of the beam was measured, Poisson's ratio ν was taken from tables in the literature [4, p. 982], and the yield strength Y (in uniaxial stress) was given by the manufacturer of the spring steel beam. The values of E and v for the steel mass (block) were taken to be the same as those for the beam. Also, the masses and dimensions of the beam and mass (block) were measured and their average densities ρ_{avg} were calculated. Table 1 summarizes this data and includes the value of the radius R. It is also noted that the average density of the mass (block) includes the influence of the screws and clamping system.

For small amplitudes and low frequencies the beam and the centroid of the mass remain in the same plane. Whereas, for other amplitudes and frequencies the centroid of the mass moves out-of-plane as the beam experiences dynamic lateral torsional buckling. Since the shear force applied by the mass on the end of the beam depends on both the amplitude ϕ_0 and frequency ω of excitation, this dynamic buckling can occur at different values of ϕ_0 and ω. One objective of these experiments is to find different values of ϕ_0 and ω where this phenomena can occur.

As previously mentioned, the specimen was designed so that this buckling occurs at frequencies which are different from the linear resonance frequencies of the system. This was done as an attempt to ensure that significant out-of-plane response was due to buckling and not merely coupling with linear modes of vibration. Also, it is necessary to consider the limitations Eq. (2.2) of the equipment.

2.1. Evaluation of the natural frequencies of the system

A simplified model was developed in order to estimate the natural frequencies of the system. Specifically, the beam was modeled as a straight, massless Bernoulli–Euler beam with length L, height h and width w. The end $x_3 = 0$ is clamped and the end $x_3 = L$ is attached to a mass such that body triad $\mathbf{e}'_i$ is oriented in the principal directions of inertia of the mass, with $\mathbf{e}'_3$ oriented tangent to the reference curve of the beam (see Fig. 3).

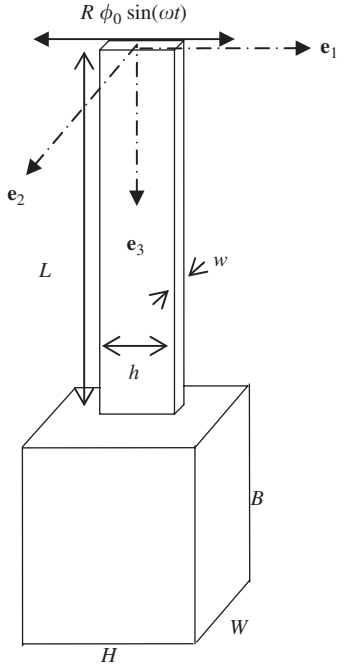

Fig. 2. Sketch of the beam-mass system.

Table 1
Measured characteristics of the beam-mass system

Beam		Mass (Block)	
L (mm)	129.0	B (mm)	30.0
h (mm)	6.0	H (mm)	15.0
w (mm)	0.50	W (mm)	15.0
m (g)	2.9	M (g)	51
ρ_{avg} (Mg/m^3)	7.50	ρ_{avg} (Mg/m^3)	7.50
R (mm)			30.0
E (Gpa)			180
v[a]			0.3
Y[a] (GPa)			2.0
g (m/s^2)			9.81

[a]The values of v and Y were determined by tables for steel.

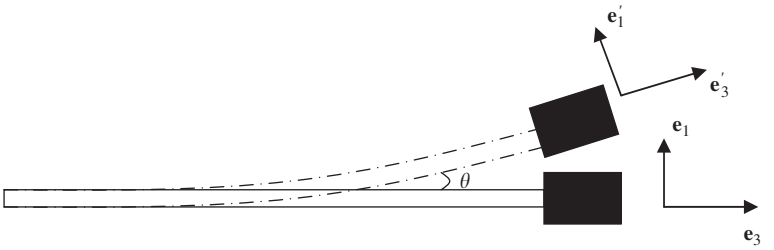

Fig. 3. Sketch of the simple model.

Within the context of the linear theory, the deformation of the end $x_3 = L$ is characterized by the displacement vector $\mathbf{u}(L)$ and the rotation vector $\boldsymbol{\theta}(L)$, such that

$$\begin{aligned}
&\mathbf{u}(L) = u_{iL}\,\mathbf{e}_i, \quad \boldsymbol{\theta}(L) = \theta_{iL}\,\mathbf{e}_i,\\
&\mathbf{e}'_1 = \mathbf{e}_1 + \theta_{3L}\,\mathbf{e}_2 - \theta_{2L}\,\mathbf{e}_3, \quad \mathbf{e}'_2 = -\theta_{3L}\,\mathbf{e}_1 + \mathbf{e}_2 + \theta_{1L}\,\mathbf{e}_3,\\
&\mathbf{e}'_3 = \theta_{2L}\,\mathbf{e}_1 - \theta_{1L}\,\mathbf{e}_2 + \mathbf{e}_3,
\end{aligned} \tag{2.3}$$

where $\mathbf{e}_i$ are fixed rectangular Cartesian base vectors and the usual summation convention is applied over repeated lower cased indices (no sum is implied over repeated upper cased indices). Appendix A derives expressions for the force $\mathbf{f}_L$ and moment $\mathbf{m}_L$ (about the centroid of the beam's cross-section) applied by the mass on the beam at its end $x_3 = L$. Specifically, this derivation yields the expressions:

$$\begin{aligned}
&\mathbf{f}_L = f_{iL}\mathbf{e}_i, \quad f_{1L} = K_{11}u_{1L} + K_{14}\theta_{2L}, \quad f_{2L} = K_{22}u_{2L} + K_{23}\theta_{1L},\\
&f_{3L} = \alpha Mg + \frac{EAu_{3L}}{L},\\
&\mathbf{m}_L = m_{iL}\mathbf{e}_i, \quad m_{1L} = K_{32}u_{2L} + K_{33}\theta_{1L}, \quad m_{2L} = K_{41}u_{1L} + K_{44}\theta_{2L},\\
&m_{3L} = \frac{B_3\theta_{3L}}{L},
\end{aligned} \tag{2.4}$$

where $A = hw$ is the cross-sectional area, B_3 is the torsional rigidity Eq. (A.9) and $K_{ij} = K_{ji}$ are constants which characterize the stiffness coefficients of the beam Eqs. (A.19)–(A.21). Since K_{ij} is symmetric is can be shown that this force and moment are consistent with an elastic system that admits a strain energy function. Moreover, the constant α is introduced to consider three orientations of the beam such that the force of gravity g (per unit mass) acts in the $\alpha\mathbf{e}_3$ direction.

Next, the equations of motion of the rigid mass can be written in the forms

$$M\mathbf{a}_c = -\mathbf{f}_L + \alpha Mg\mathbf{e}_3, \quad \dot{\mathbf{H}} = -\mathbf{m}_L + \mathbf{x}_{b/c} \times (-\mathbf{f}_L), \tag{2.5}$$

where $\mathbf{a}_c$ is the absolute acceleration of the center of mass c, $\mathbf{H}$ denotes the angular momentum of the mass (block) about its center of mass, a superposed dot denotes time differentiation, and $\mathbf{x}_{b/c}$ denotes the location of the centroid of the end of the beam relative to the center of mass c,

$$\mathbf{x}_{b/c} = -\frac{\mathrm{B}}{2}\mathbf{e}_3'. \tag{2.6}$$

Now, for small deformations the acceleration $\mathbf{a}_c$ and the angular momentum $\boldsymbol{H}$ can be expressed in the forms

$$\begin{aligned}
&\mathbf{a}_c = \ddot{u}_{iL}\mathbf{e}_i + \ddot{\boldsymbol{\theta}} \times \frac{B}{2}\mathbf{e}_3' = \left[\ddot{u}_{1L} + \frac{B}{2}\ddot{\theta}_{2L}\right]\mathbf{e}_1 + \left[\ddot{u}_{2L} - \frac{B}{2}\ddot{\theta}_{1L}\right]\mathbf{e}_2 + [\ddot{u}_{3L}]\mathbf{e}_3,\\
&\mathbf{H} = I_1\dot{\theta}_{1L}\mathbf{e}_1 + I_2\dot{\theta}_{2L}\mathbf{e}_2 + I_3\dot{\theta}_{3L}\mathbf{e}_3,
\end{aligned} \tag{2.7}$$

where the moments of inertia $\{I_1, I_2, I_3\}$ about the center of mass c are given by

$$I_1 = \frac{M}{12}(W^2 + B^2), \quad I_2 = \frac{M}{12}(H^2 + B^2), \quad I_3 = \frac{M}{12}(H^2 + W^2). \tag{2.8}$$

Thus, with the help of Eqs. (2.4) and (2.7), the equations of motion, i.e. Eq. (2.5) reduce to

$$\begin{aligned}
&M\left[\ddot{u}_{1L} + \frac{B}{2}\ddot{\theta}_{2L}\right] + K_{11}u_{1L} + K_{14}\theta_{2L} = 0,\\
&M\left[\ddot{u}_{2L} - \frac{B}{2}\ddot{\theta}_{1L}\right] + K_{22}u_{2L} + K_{23}\theta_{1L} = 0,\\
&M[\ddot{u}_{3L}] + \left[\frac{EAu_{3L}}{L}\right] = 0,\\
&I_1\ddot{\theta}_{1L} + \left[\frac{B}{2}K_{22} + K_{32}\right]u_{2L} + \left[\frac{B}{2}(K_{23} + \alpha Mg) + K_{33}\right]\theta_{1L} = 0,\\
&I_2\ddot{\theta}_{2L} + \left[-\frac{B}{2}K_{11} + K_{41}\right]u_{1L} + \left[-\frac{B}{2}(K_{14} - \alpha Mg) + K_{44}\right]\theta_{2L} = 0,\\
&I_3\dot{\theta}_{3L} + \left[\frac{B_3\theta_{3L}}{L}\right] = 0,
\end{aligned} \tag{2.9}$$

where the effect of gravity it considered to be finite and quadratic expressions in the quantities $\{\theta_{1L}, \theta_{2L}, f_{1L}, f_{2L}\}$ have been neglected. These equations separate into two sets of coupled equations for the shear and bending in terms of the variables $\{u_{1L}, \theta_{2L}\}$ and $\{u_{2L}, \theta_{1L}\}$, and two uncoupled equations for axial extension u_{3L} and torsion θ_{3L}. For design purposes the effect of gravity was neglected ($\alpha = 0$) and the eigenvalue problem associated with Eq. (2.9) gives the natural frequencies and mode shapes recorded in Table 2. From this table it can be seen that Modes 1–6 characterize, respectively, the first mode of bending in the weak plane,

Table 2
Natural frequencies and mode shapes of the simple Bernoulli–Euler model (ignoring the effect of gravity $\alpha = 0$)

Mode	1	2	3	4	5	6
Frequency (Hz)	2.45	28.4	41.2	51.1	613	1447
Amplitude of u_{1L}	0	0.08	0	0	−0.016	0
Amplitude of u_{2L}	0.08	0	0	0.016	0	0
Amplitude of u_{3L}	0	0	0	0	0	1
Amplitude of θ_{1L}	1	0	0	1	0	0
Amplitude of θ_{2L}	0	1	0	0	1	0
Amplitude of θ_{3L}	0	0	1	0	0	0

the first mode of bending in the stiff plane, torsion, the second mode of bending in the weak plane, the second mode of bending in the stiff plane, and axial extension.

2.2. Estimation of the buckling frequency

Next, it is necessary to estimate the frequency at which dynamic lateral torsional buckling can occur. Assuming that the beam remains rigid, the magnitude P of the shear force applied by the mass (block) on the beam can be estimated by using the magnitude of the tangential acceleration of its center of mass to obtain

$$P = M\phi_0\omega^2\left[R + L + \frac{B}{2}\right]. \tag{2.10}$$

A lower bound for buckling to occur is obtained by equating this magnitude to the magnitude P_{cr} required for static buckling [1]

$$P_{cr} = 4.0126\frac{\sqrt{I_{22}EB_3}}{L^2}. \tag{2.11}$$

Plastic failure of the beam at its base will occur when the tensile stress reaches the yield stress Y of the beam. Thus, to eliminate yielding the shear force P must remain below the value P_p given by

$$P_p = \frac{2YI_{11}}{hL}. \tag{2.12}$$

The properties of the beam-mass system given in Table 1 were specified to meet the design criterion. Fig. 4 plots the design curves of P/P_{cr} and P/P_p versus the frequency for the amplitude $\phi_0 = 0.65^\circ$ and the properties in Table 1. From this figure it can be seen that buckling will occur above the value of frequency $\omega = 20.4$ Hz (associated with $P/P_{cr} = 1$) and that plastic failure will not occur ($P/P_p < 1$) in the range of frequencies being considered.

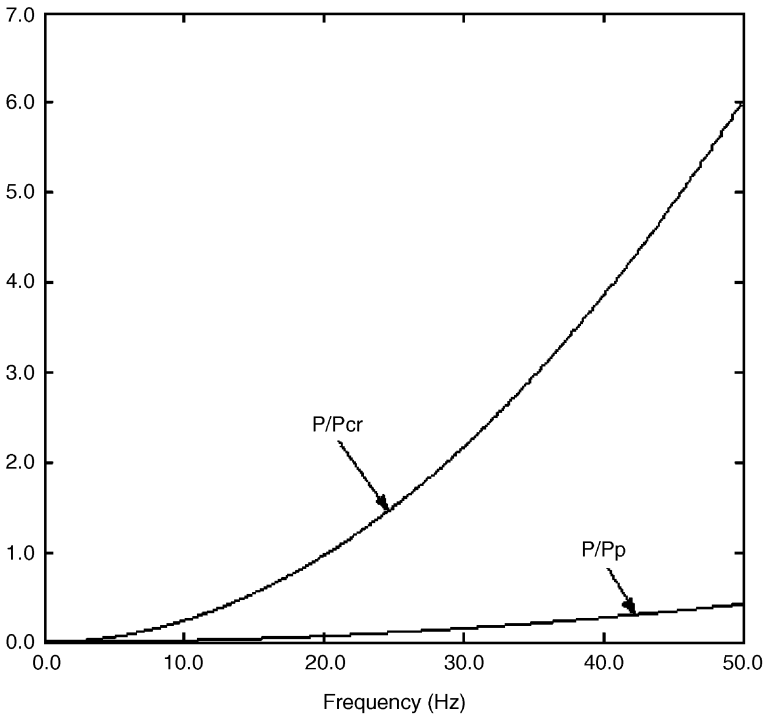

Fig. 4. Design curves for predicting the onset of buckling and plastic failure for the amplitude $\phi_0 = 0.65^\circ$ and the properties in Table 1.

2.3. Effect of gravity

As mentioned, the effect of gravity was ignored in designing the specimen. However, once the experimental setup was built, the accuracy of the simple model Eq. (2.9) was examined. Specifically, the frequency of the first mode of bending in the weak bending plane was measured to be 2.76 Hz which is quite different from the value of 2.45 Hz predicted in Table 2. After rechecking the dimensions of the beam and its mechanical properties it was realized that gravity has a significant effect on the natural frequency. In particular, measurements of the first natural frequency in bending were made by positioning the beam in three different positions: (i) with the mass below the beam's clamped end ($\alpha = 1$); (ii) with the beam being horizontal (approximated by $\alpha = 0$); and (iii) with the mass above the beam's clamped end ($\alpha = -1$). Table 3 shows that when the effect of gravity is included in the simple theory Eq. (2.9), the predictions of this bending frequency compare reasonably well with the experimental data. Unless otherwise stated, the experiments reported below refer to the orientation $\alpha = 1$ where the mass is located below the beam's clamped end.

3. Response to a swept-sine loading

In order to study the behavior of the system it is convenient to use a swept-sine (CHIRP) input which is characterized by constant amplitude and a frequency that increases linearly with time in a specified frequency range. The digital signal processor (DSP) controlling the motor in the experimental system was programmed to supply this input. Specifically, the amplitude was set to 0.65° and the frequency range was taken to be 0–40 Hz with a sweeping time of 30 s. Use of the CHIRP input in conjunction with a suitable time–frequency analysis [5] made it relatively easy to identify frequency ranges where dynamic buckling occurs. Moreover, analysis of the response helped identify that the controller had difficulties maintaining a constant high amplitude, especially when dynamic buckling occurred. Consequently, the excitation of the beam during dynamic buckling was not exactly a pure sine function as specified by Eq. (2.1). In this regard, it is also noted that controlling nonlinear flexible structures to undergo a nearly perfect sinusoidal motion remains a difficult challenge. A special difficulty of the particular experimental setup used here is that the nonlinear buckling takes place in a mode that is nearly orthogonal to the small deformation mode caused by rotation of the motor shaft. Consequently, the controller has limited success in controlling a sinusoidal amplitude of rotation when buckling occurs.

The CHIRP output signal of the signal processor, the encoder reading of the rotation of the motor shaft, and the laser sensor reading of the velocity of the mass were recorded during each of the CHIRP experiments. A continuous Gabor transform, also known as the short-time Fourier transform, was used to construct the time–frequency distribution (TFD) [6] with which the measured response signals were analyzed. This distribution analyzes the energy content of the signal as a function of the evolving frequency of excitation. Figs. 5a,b show the TFD for two periods of loading (each of which starts at zero frequency) of the encoder readings and the laser sensor measurements in the $\mathbf{e}_2$ direction, respectively. These figures give plots of frequency versus time with intensity indicating the energy level of the specific frequency component. The bold diagonal lines of the encoder readings in Fig. 5a indicate that the controller causes the motor shaft to follow the CHIRP input, but due to the strong coupling with the nonlinear dynamics, integer multiples of the excitation frequency (the other diagonal lines in Fig. 5a) are excited as well. The gaps in the diagonal bold lines in Fig. 5a indicate that the controller cannot maintain a constant amplitude near an input frequency of about

Table 3
Effect of gravity

α	Measured frequency (Hz)	Theory frequency (Hz)
1	2.76	2.73
0	2.35	2.45
−1	1.87	2.07

Measured natural frequencies of the first bending mode in the weak bending plane and theoretical predictions of the simple model Eq. (2.9) for different values of α.

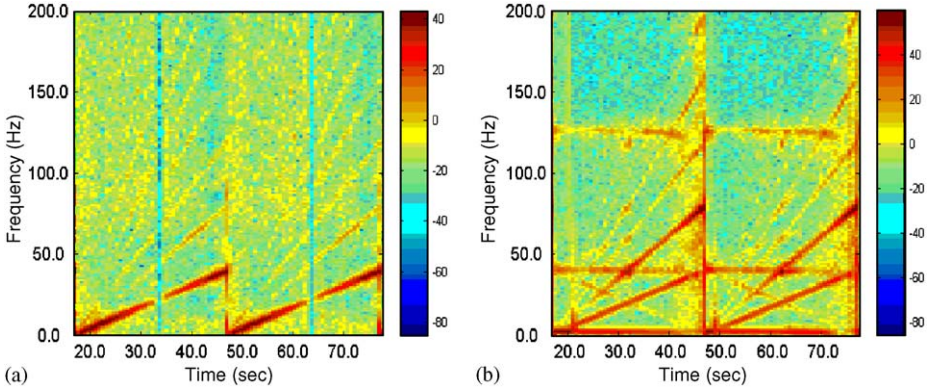

Fig. 5. Time–frequency distribution response to a CHIRP excitation: (a) encoder readings and (b) laser sensor readings.

35.0 Hz. This is consistent with the experimental observation that dynamic buckling occurred near 35.0 Hz with the mass beginning to twist instead of merely vibrating with the weakest bending mode. Consequently, at this point most of the vibrational energy has been converted into torsional vibrations around $\mathbf{e}_3$ (associated with dynamic bucking) and the motor torque produces little vibration in the $\mathbf{e}_2$ direction. In Fig. 5a it can also be observed that a surge in the rotational vibration occurs at a frequency of around 40 Hz (associated with the small deformation torsional mode in Table 12). Some of the horizontal lines in the TFD of the laser sensor readings in Fig. 5b indicate the natural frequencies of the system. The first weak bending mode occurs at about 2.8 Hz and the torsional mode occurs at about 40 Hz. These results are reasonably close to the predictions of the simple model (2.9) in Tables 2, 3 and 12. Furthermore, it is instructive to observe the dark regions where the angular vibrations become high. These points either indicate excitation of natural frequencies by integer multiples of the CHIRP input or they are a transient artifact.

The CHIRP experiment was conducted with an amplitude of 0.65° and the phenomena of dynamic lateral torsional buckling was observed at a frequency of 35.0 Hz. Additional experiments were conducted to determine whether the phenomena also occurs at other frequencies and amplitudes. In order to keep the force exerted by the mass on the beam sufficiently high as the frequency was decreased the amplitude was increased.

Fig. 6 shows three sets of responses for different excitation amplitudes ϕ_0 and frequencies ω. Three frames (separated by 4 s each) from a high resolution video are presented for each excitation. With reference to this figure, the first set of three frames ($\phi_0 = 0.65^\circ$ and $\omega = 35.0$ Hz) will be called Torsion I, the second set of three frames ($\phi_0 = 1.49^\circ$ and $\omega = 25.5$) will be called Torsion III and the third set of three frames ($\phi_0 = 0.65^\circ$ and $\omega = 35.0$ Hz) will be called Bending II. An additional experiment called Torsion II ($\phi_0 = 1.50^\circ$ and $\omega = 27.0$ Hz) will be discussed later. For Torsion I dynamic lateral torsional buckling occurs as the beam remains bent to one side while the mass twists. The response of Torsion III shows that this same buckling phenomena can be produced at a different excitation amplitude and frequency. Similar buckling phenomena (like Torsion II) were observed at other amplitudes and frequencies which are not shown. In general, it was found that the amplitude of the out-of-plane displacement of the mass increases as the excitation amplitude increases and the frequency decreases. For a fixed amplitude and increasing frequency, it was observed that oscillations of the mass in the weakest plane of bending of the beam occur for frequencies both below and above a critical frequency at which the out-of-plane deflection of the mass remains relatively constant. A similar response is observed when the frequency is fixed and the amplitude is increased. It should be noted that this pattern of oscillation is stable and persists until the frequency or amplitude are adjusted out of a certain range. The limits of this range were not explored in detail.

Comparison of Torsion I and Bending II in Fig. 6 indicates that two different modes of oscillation occur at the same excitation ($\phi_0 = 0.65^\circ$ and $\omega = 35.0$ Hz). Specifically, in Bending II the mass rotates about its nearly fixed center of mass as the beam deforms with its second bending mode in its weak-bending plane. A snap-through-type bending occurs as the beam becomes nearly straight (see the center frame of Bending II). This mode also persists unless the mass is deflected slightly out-of-plane causing the mode to transition to that associated with Torsion I in Fig. 6.

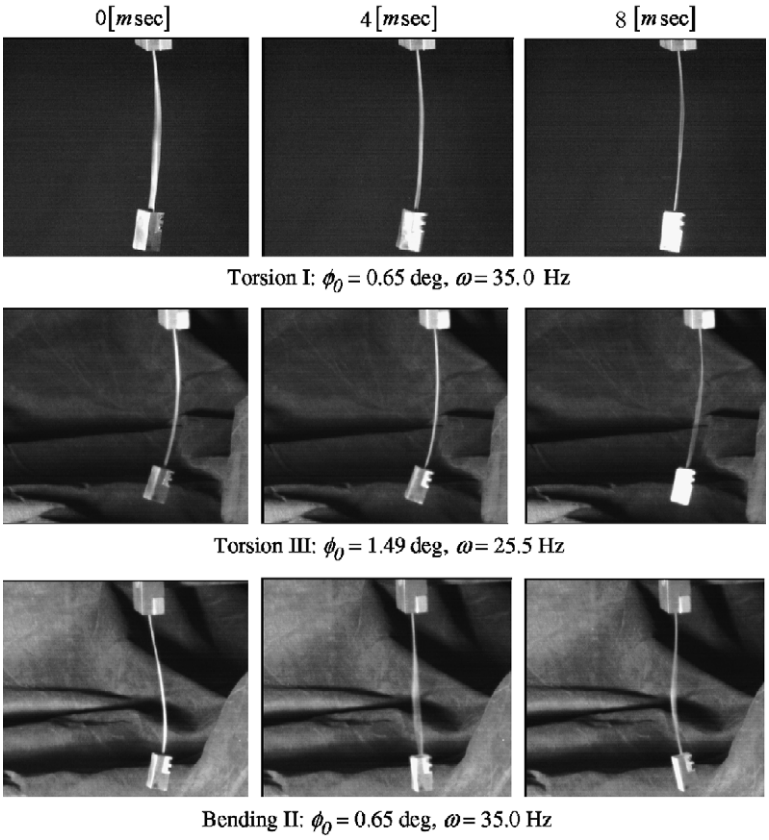

Fig. 6. Three sets of responses (Torsion I, Torsion III and Bending II) for different excitation amplitudes and frequencies.

4. Laser sensor scanning method for measuring torsion

One of the methods used here for measuring the amplitude and frequency of torsion of the beam employed a continuous laser scan of the mass. Fig. 7 shows a sketch of this laser sensor scanning method. The laser beam measures the velocity in the $\mathbf{e}_2$ direction of points on the surface of the mass. This velocity component is influenced by both the translational and rotational motion of the mass as well as by the fact that the laser beam does not track a specific material point on the mass.

For this method it is assumed that the mass experiences quasi-periodic, two-dimensional motion in the $\mathbf{e}_1$–$\mathbf{e}_2$ plane which is dominated by a component with frequency ω. The center of the line representing the surface of the mass moves to the position $\mathbf{x}_0(t)$ and the line rotates with angle $\theta(t)$ about the $\mathbf{e}_3$ axis. For small displacements and angles, the dominant part of the new position $\mathbf{x}$ of a material point X on this line is given by

$$\begin{aligned}
\mathbf{x}(X,t) &= x(X,t)\mathbf{e}_1 + y(X,t)\mathbf{e}_2 = X\mathbf{e}_1 + \mathbf{x}_0(t) + \theta(t)X\mathbf{e}_2,\\
\mathbf{x}_0 &= X_0\cos(\omega t+\xi)\mathbf{e}_1 + Y_0\cos(\omega t+\psi)\mathbf{e}_2, \quad \theta = \theta_0\cos(\omega t+\tau),\\
x(X,t) &= X + X_0\cos(\omega t+\xi), \quad y(X,t) = Y_0\cos(\omega t+\psi) + \theta(t)X,
\end{aligned} \tag{4.1}$$

where X is the distance of a material point on the line from its center, $\{X_0, Y_0, \theta_0\}$ are amplitudes and $\{\xi, \psi, \tau\}$ are phase angles. It follows that the velocity v of a material point in the $\mathbf{e}_2$ direction is given by

$$v(X,t) = \dot{y}(X,t) = -\omega[Y_0\sin(\omega t+\psi) + \theta_0 X\sin(\omega t+\tau)]. \tag{4.2}$$

This velocity field can also be written in the Eulerian form

$$v(x,t) = -\omega[Y_0\sin(\omega t+\psi) + \theta_0 x\sin(\omega t+\tau)], \tag{4.3}$$

since the product $\theta_0 X_0$ does not affect the laser sensor's output [7].

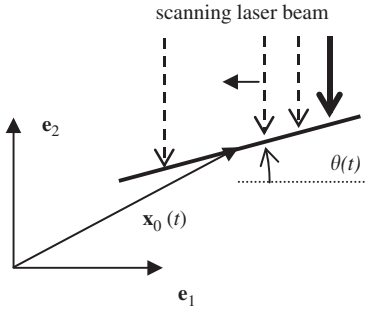

Fig. 7. Sketch of the laser sensor scanning method for measuring torsion.

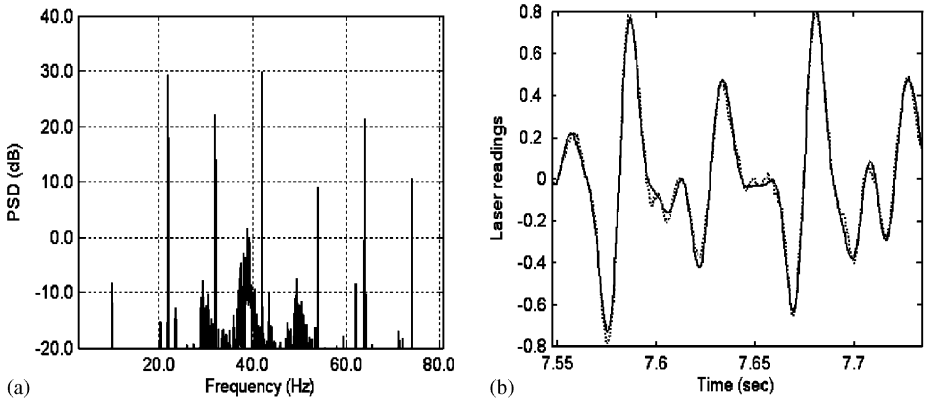

Fig. 8. Data from one of the tests used to measure the torsion angle: (a) power spectral density (PSD) and (b) comparison of the measurements with the parametric function for the velocity. The curve labels are: (—) Par.; (· · · · ·) Exp.

In order to separate the effects of translation and rotation of the mass, the spatial position of the laser beam is modulated according to the formula

$$x = A\,\sin(\Omega t + \delta), \tag{4.4}$$

where Ω is the scanning frequency, A is the amplitude and δ is the phase angle. It therefore follows that the velocity $v_L(t)$ measured by the laser sensor is given by substituting Eq. (4.4) into Eq. (4.3) to obtain

$$v_L(t) = -\omega[Y_0\,\sin(\omega t + \psi) + \theta_0 A\,\sin(\Omega t + \delta)\,\sin(\omega t + \tau)]. \tag{4.5}$$

Next, using standard trigonometric relations this expression can be rewritten in the form

$$v_L(t) = \frac{\omega\theta_0 A}{2}[\cos\{(\omega + \Omega)t + \tau + \delta\} - \cos\{(\omega - \Omega)t + \tau - \delta\}] - \omega Y_0\,\sin(\omega t + \psi). \tag{4.6}$$

It now can be seen from this equation that the angular motion is shifted to two sidebands having the frequencies $\omega \pm \Omega$, respectively. These sidebands have the same amplitudes ($\omega\theta_0 A/2$) but different phases ($\tau + \delta$ and $\tau - \delta$, respectively).

A series of tests were conducted at discrete frequencies in the interval 31.0–34.0 Hz with steps of 0.5 Hz. Fig. 8a shows the power spectral density (PSD) of the steady-state data taken from one of the tests for which $\omega = 31$, $\Omega = 10.0$ Hz and $A = 5$ mm. The amplitudes of the sidebands in Fig. 8a at $\omega - \Omega = 21$ and $\omega + \Omega = 41$ Hz can be seen to be the same in accordance with the result Eq. (4.6). From Fig. 8a it can also been seen that integer multiples of the excitation frequency ω have sidebands with similar amplitudes.

Next, the method of least squares was used to determine the best values of $\{\theta_0, Y_0, \tau, \delta, \psi\}$ in the expression Eq. (4.6) which fit the experimental data. Fig. 8b shows that the resulting analytical curve fits the experimental

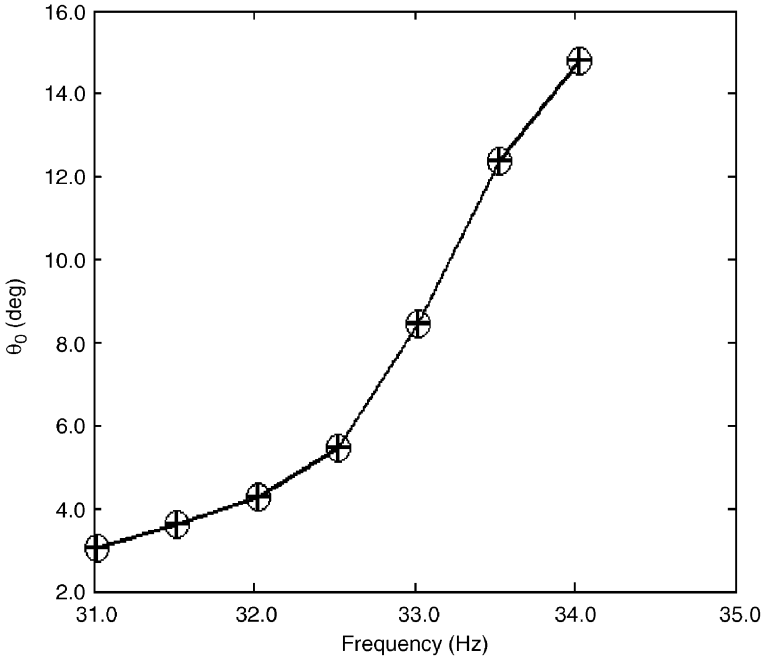

Fig. 9. Amplitude of the torsion angle versus excitation frequency. The curve labels are: (–+–) ω–Ω; (–o–) $\omega + \Omega$.

data for velocity quite well. Moreover, using this procedure for the other tests it is possible to determine the torsion amplitude θ_0 for the data of both of the main sidebands and the results are presented in Fig. 9. In particular, it can be seen that the torsion amplitude is a nonlinear function of the excitation frequency. Moreover, it is noted that this scanning procedure becomes inaccurate for large deformations of the beam-mass system since the assumption of two-dimensional motion of the mass no longer holds.

5. Image processing method for measuring amplitudes

As mentioned previously, a high speed digital video camera was used to photograph some of the experiments. Although the camera is capable of taking up to 1000 frames per second (fps), the framing rate had to be reduced to around 250 fps when using a large opening angle to photograph the entire beam-mass system.

The video for the Torsion I response shown in Fig. 6 was processed using edge detection methods. Fig. 10 shows a sketch of the analysis of the edges of a cross-section of the beam. Each frame of the videos was rotated by a fixed angle to ensure that the clamped edge of the beam was vertical so that measurements from the edge of the rotated picture would be parallel to the $\mathbf{e}_2$ axis. The distances $\{y_B, y_F\}$ from the edge of the rotated frame to the back and front edges, respectively, of the beam are measured at the same deformed axial location $x_3 = z$ from the beam's clamped end. Then, the location y of the centerline of the beam is determined by the expression

$$y = \tfrac{1}{2}(y_B + y_F). \tag{5.1}$$

Due to the camera angle it is not possible to accurately measure displacements in the $\mathbf{e}_1$ direction. Moreover, in obtaining a value for the torsion angle it is necessary to account for the fact that the mass is oriented at an angle to the vertical. Therefore, for the measurement of the torsion angle each of the frames in the video was rotated by the same angle (different from that used to measure the centerline) to cause the edges of the mass to become vertical. Then, the new horizontal distances $\{\bar{y}_B, \bar{y}_F\}$ from the edge of the rotated frame to the back and front edges, respectively, of the mass were measured. Using these values and the fact that the true distance between these edges is H, it is possible to obtain an approximate value θ of the

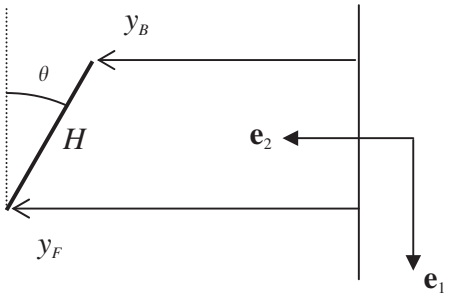

Fig. 10. Analysis of the edges of the cross-section of the beam.

torsion angle using the formula

$$\theta = \sin^{-1}\left(\frac{\bar{y}_F - \bar{y}_B}{H}\right). \tag{5.2}$$

Furthermore, since the mass is nearly rigid this angle is considered to be the torsion angle at the beam's end attached to the mass.

The data from this edge detection procedure is analyzed using two different methods. The first method uses a parametric model to curve-fit the time response of the data at a specified axial location. The second method uses a polynomial function to approximate the spatial shape of the beam at a specified time. Due to the small differences in the locations of the edges of the beam, the torsion angle in the beam region was too noisy to be measured accurately. Therefore, only the parametric model is developed for the torsion angle at the beam's end attached to the mass, since it relies on a large number of frames to overcome the effects of quantization due to the coarse image resolution. The inevitable random noise, generates a natural dither in the quantized measurements thus enabling a statistical improvement of the spatial resolution due to the parametric approach [8].

In order to determine a parametric model for the motion of the beam from the converted film it is necessary to first determine an accurate value of the frequency of motion. To this end, the coordinate y of the beam's centerline at a specified axial location was recorded to obtain an array of coordinates y_i at times t_i associated with M frames. Then, the resulting data was approximated by a Fourier series

$$y(t) = \sum_{n=0}^{N} [a_n \sin(n\omega t) + b_n \cos(n\omega t)], a_0 = 0, \tag{5.3}$$

where the $(2N+2)$ constants $\{a_n, b_n, \omega\}$ are determined by approximating the M equations

$$y(t_i) = y_i \text{ for } i = 1, 2, \ldots, M. \tag{5.4}$$

Since the number of equations M is much larger than the number of unknowns $(2N+2)$, the system of equations is over determined. Here, the system Eq. (5.4) is solved in the least-squares sense. Specifically, a two stage approach is employed. In stage 1 the frequency ω is curve fitted to the constant amplitude excitation signal. Once ω is found, a set of over determined linear equations is solved for $\{a_n, b_n\}$ using a linear least-squares approach. This process (with $N = 3$) was performed for one point on the beam located by its deformed axial position z and the parametric frequency determined associated with this point was very close to the excitation frequency $\omega = 35.0$ Hz specified by the controller.

Next, edge detection was used to quantify the locations of the centerline of a number of points along the axis of the beam in each frame of the movie. This yields an array of locations y_{ij} and times t_i and axial locations $z = z_j$. Parametric functions for the motion at each axial location z_j can be expressed in the forms

$$y_j(t) = \sum_{n=0}^{N} [a_{nj} \sin(n\omega t) + b_{nj} \cos(n\omega t)], \quad a_{0j} = 0, \tag{5.5}$$

Table 4a
Torsion I—the beam's centerline: values of the constants in the parametric approximation Eq. (5.5) for $\omega = 35.0$ Hz and different deformed axial locations z from the beam's clamped end

z (mm)	b_0 (mm)	a_1 (mm)	b_1 (mm)	a_2 (mm)	b_2 (mm)	a_3 (mm)	b_3 (mm)
48	0.62158	0.11661	−0.32507	0.03598	0.026836	0.065451	0.10686
64	−0.79209	0.25296	−0.45071	−0.33912	−0.11817	0.070966	0.28214
80	−2.3806	0.1084	−0.63024	−0.54603	−0.27617	0.08873	0.055645
96	−4.2345	0.065247	−0.75894	−0.62671	−0.45833	0.003012	−0.0441
111	−6.2633	−0.0524	−0.69462	−0.65511	−0.53358	−0.0241	−0.08402
127	−8.9525	−0.15525	−0.51063	−0.50555	−0.4786	−0.02015	−0.11183

Table 4b
Torsion I—the beam's centerline: values of the constants in the polynomial approximation Eq. (5.7) for different times t

t (ms)	d_0 (mm)	d_1 (mm)	d_2 (mm)	d_3 (mm)	d_4 (mm)	d_5 (mm)
0	0.27737	1.5959	34.062	−161.75	188.65	−73.250
9	0.089548	0.18971	45.692	−183.87	212.42	−83.715
21	−0.09828	−1.2181	57.600	−206.45	236.12	−94.307

Table 5
Torsion I—the torsion angle: values of the constants in the parametric approximation Eq. (5.5) for $\omega = 35.0$ Hz and the deformed axial location $z = 127$ mm from the beam's clamped end

b_0 (deg)	a_1 (deg)	b_1 (deg)	a_2 (deg)	b_2 (deg)	a_3 (deg)	b_3 (deg)
0.0305	24.0159	9.7192	4.6552	5.9121	0.0395	0.2202

Table 6a
Torsion II—the beam's centerline: values of the constants in the parametric approximation Eq. (5.5) for $\omega = 27.0$ Hz and different deformed axial locations z from the beam's clamped end

z (mm)	b_0 (mm)	a_1 (mm)	b_1 (mm)	a_2 (mm)	b_2 (mm)	a_3 (mm)	b_3 (mm)
40	0.3568	−0.3929	0.2001	0.6557	−0.1011	−0.0269	−0.5943
56	0.5319	−0.5813	0.3756	1.2374	−0.163	−0.0771	−2.8538
72	0.6163	−0.6794	0.4535	1.6064	−0.2516	−0.1311	−5.6742
88	0.5738	−0.6397	0.4195	1.5127	−0.262	−0.1519	−9.2041
104	0.9791	−1.6172	0.0717	0.387	−0.2354	0.0035	−9.0206

Table 6b
Torsion II—the beam's centerline: values of the constants in the polynomial approximation Eq. (5.7) for different times t

t (ms)	d_0 (mm)	d_1 (mm)	d_2 (mm)	d_3 (mm)	d_4 (mm)	d_5 (mm)
0	0.0775	0.2555	44.6147	−225.992	305.3372	−155.624
12	0.0508	1.7192	32.0918	−235.031	345.1034	−172.248
24	0.024	3.1829	19.5688	−244.07	384.8696	−188.872

Table 7
Torsion II-the torsion angle: values of the constants in the parametric approximation Eq. (5.5) for $\omega = 27.0$ Hz and the deformed axial location $z = 110$ mm from the beam's clamped end

z (mm)	b_0 (deg)	a_1 (deg)	b_1 (deg)	a_2 (deg)	b_2 (deg)	a_3 (deg)	b_3 (deg)
110	12.1283	3.1278	−4.0187	−3.9420	−1.4618	−0.8546	−1.1189

Table 8a
Torsion III—the beam's centerline: values of the constants in the parametric approximation Eq. (5.5) for $\omega = 25.5$ Hz and different deformed axial locations z from the beam's clamped end

z (mm)	b_0 (mm)	a_1 (mm)	b_1 (mm)	a_2 (mm)	b_2 (mm)	a_3 (mm)	b_3 (mm)
48	−1.2643	0.4237	0.2413	−0.7374	−0.4377	0.0691	0.0987
64	−3.8979	0.6288	0.3932	−1.1398	−0.7393	0.1448	0.0893
60	−3.2507	0.5747	0.3738	−1.0559	−0.654	0.1003	0.1126
96	−10.766	0.7577	0.4874	−1.314	−0.8899	0.2259	0.1325
111	−15.756	0.8394	−0.6464	−0.0375	−0.2046	0.0584	0.7769
127	−18.328	2.0728	0.8815	0.3841	0.4986	0.2329	0.041

Table 8b
Torsion III—the beam's centerline: values of the constants in the polynomial approximation Eq. (5.7) for different times t

t (ms)	d_0 (mm)	d_1 (mm)	d_2 (mm)	d_3 (mm)	d_4 (mm)	d_5 (mm)
0	−0.2179	0.7172	47.574	−260.90	335.42	−144.88
13	−0.0008	0.0943	42.380	−234.20	302.56	−133.95
26	0.2164	−0.5287	37.187	−207.51	269.69	−123.01

Table 9
Torsion III—the torsion angle: values of the constants in the parametric approximation Eq. (5.5) for $\omega = 25.5$ Hz and the deformed axial location $z = 110$ mm from the beam's clamped end

z (mm)	b_0 (deg)	a_1 (deg)	b_1 (deg)	a_2 (deg)	b_2 (deg)	a_3 (deg)	b_3 (deg)
110	7.8284	17.945	11.410	−2.3822	−15.231	0.0634	−2.8656

Table 10a
Bending II—the beam's centerline: values of the constants in the parametric approximation Eq. (5.5) for $\omega = 35.0$ Hz and different deformed axial locations z from the beam's clamped end

z (mm)	b_0 (mm)	a_1 (mm)	b_1 (mm)	a_2 (mm)	b_2 (mm)	a_3 (mm)	b_3 (mm)
40	−0.8029	2.3518	3.5554	−0.2561	0.2432	0.0019	0.0136
56	−0.7942	3.5027	5.4184	−0.4112	0.5911	0.0261	0.0326
72	−0.6604	4.1422	6.3819	−0.6577	0.7789	0.0878	0.0864
88	−0.6734	3.85	6.1179	−0.5715	0.9387	−0.1014	0.0458
104	−0.7338	2.9223	4.852	−0.5342	0.8553	−0.1222	0.0817
120	−5.1022	1.9214	2.2739	−0.0763	0.3137	0.2967	0.2282

Table 10b
Bending II—the beam's centerline: values of the constants in the polynomial approximation Eq. (5.7) for different times t

t (ms)	d_0 (mm)	d_1 (mm)	d_2 (mm)	d_3 (mm)	d_4 (mm)	d_5 (mm)
0	0.0207	9.7017	−29.631	230.88	−407.20	200.35
7	0.032	6.4900	−46.523	229.50	−361.96	177.38
14	0.0547	0.06756	−79.754	226.27	−271.47	130.17
21	0.066	−3.1452	−96.370	224.42	−226.23	106.17

Table 11
Bending II—the torsion angle: values of the constants in the parametric approximation Eq. (5.5) for $\omega = 35.0$ Hz and the deformed axial location $z = 127$ mm from the beam's clamped end

b_0 (deg)	a_1 (deg)	b_1 (deg)	a_2 (deg)	b_2 (deg)	a_3 (deg)	b_3 (deg)
0.0008	−0.9946	−0.7425	−1.7814	−1.2672	0.1097	0.0235

where $\omega = 35.0$ Hz and the constants $\{a_{nj}, b_{nj}\}$ need to be determined by approximating the equations

$$y_j(t_i) = y_{ij}. \tag{5.6}$$

Although different numbers of harmonics could be used for each digitized point, here N was specified to be the same for all points ($N = 3$). With the value of ω specified, the equations Eq. (5.6) are linear in the constants $\{a_{nj}, b_{nj}\}$ and they can be solved using a linear least-squares approach.

The parametric function Eq. (5.5) tends to smooth the time response at the axial location z_j. Alternatively, it is possible to use a polynomial expansion in space to smooth the deflection of the beam at each time t_i. Specifically, at each time t_i the edge detection data is fitted to the polynomial expansion

$$y_i(z) = \sum_{n=0}^{P} \mathrm{d}_n \left(\frac{z}{L}\right)^n, \tag{5.7}$$

where P denotes the order of the polynomial and the constants d_n are determined by using a linear least-squares approach to solve the over determined system of equations

$$y_i(z_j) = y_{ij} \tag{5.8}$$

for each time t_i. For the analysis below P was set equal to 5. Also, since only the relative values of the location of the centerline and the torsion angle are of interest, constants have been added to the parametric functions to produce near zero centerline displacement and zero torsion angle at the beam's clamped. Furthermore, this procedure was used to determine a parametric model for the torsion angle θ at the beam's clamped end.

The procedure just described was also applied to the data for Torsion III and Bending II in Fig. 6 as well as for the additional experiment Torsion II and the results of the analysis are presented in Figs. 11–14 and in Tables 4–11. Specifically, Fig. 11 presents the results for Torsion I with the bending of the center line given in Figs. 11a–c and the torsion angle given in Figs. 11d,e. The deformed axial location $z = 127$ mm was used for both the centerline and the torsion angle which yield the parametric frequencies very close to the excitation frequency $\omega = 35.0$ Hz that was used in the parametric functions Eq. (5.3). This axial location represents the deformed location of the beam's end which is attached to the mass so its value is different from the undeformed value $z = 129$ mm. Figs. 11a,d show that the parametric functions fit the measured data reasonably well. Figs. 11b,e show that the power spectral density of the measured data contains significant energy content at frequencies which are multiples of the excitation frequency $\omega = 35.0$ Hz. Fig. 11c compares the shapes of the beam's centerline predicted by the parametric functions and the polynomial approximation Eq. (5.7) at different times. From the results in this figure near the beam's clamped end it can be seen that the error in the edge detection method is about ± 0.25 mm since this end should not move. Details of the constants

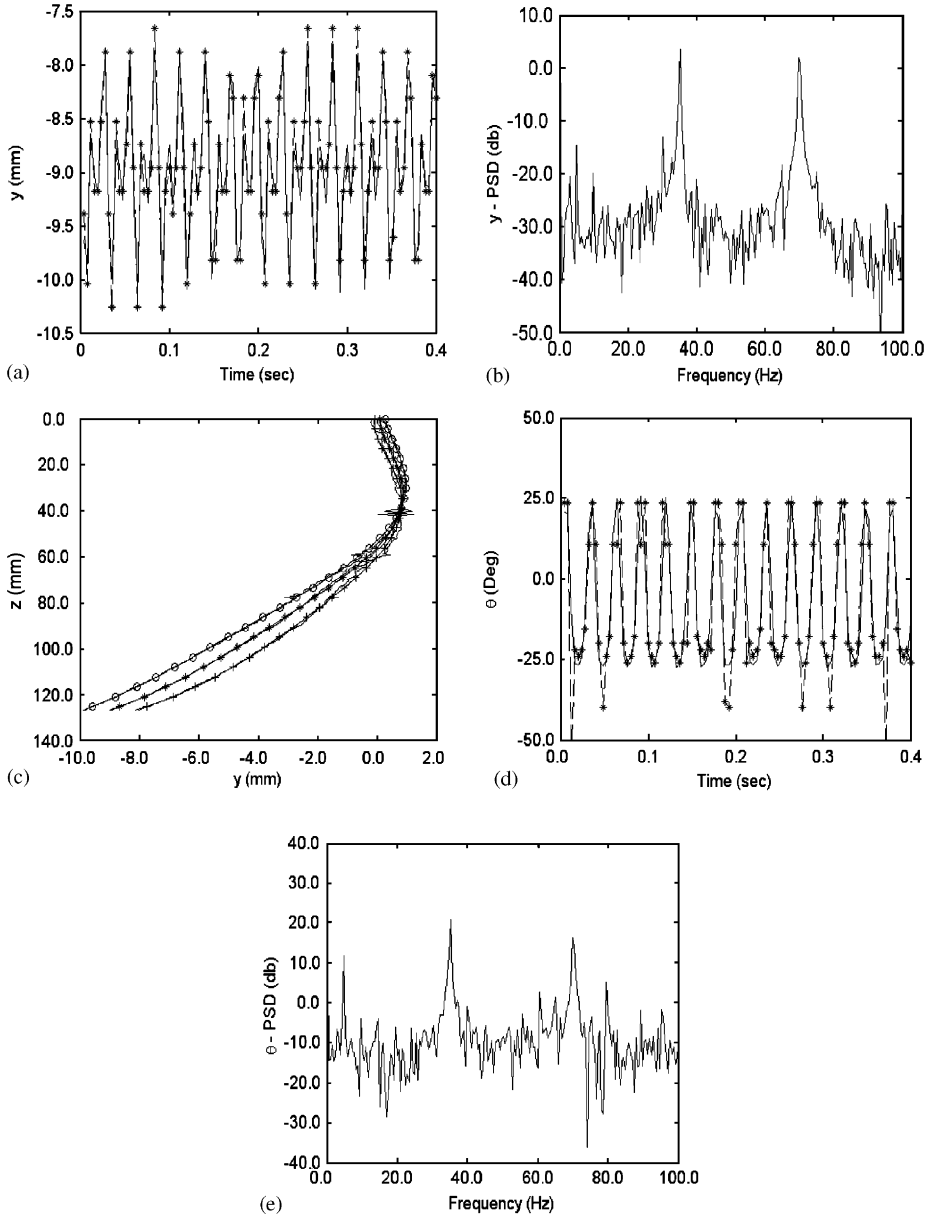

Fig. 11. Response of Torsion I for the centerline (a, b, c) and the torsion angle (d, e). For the time responses (a, b, d, e, with $N = 3$) the deformed axial location is $z = 127$ mm. Also, the spatial shapes (c, with $P = 5$) are presented for different times. The curve labels are: (a, d) (–∗–) Exp.; (—) Par.; (c) (–o–) 0 (ms); (–∗–) 9 (ms); (–+–) 18 (ms).

in both the parametric and polynomial approximations for Torsion I can be found in Tables 4 and 5. This data is provided to allow for future validation of analytical or numerical models.

Fig. 12 and Tables 6 and 7 analyze the Torsion II response and Fig. 13 and Tables 8 and 9 analyze the Torsion III response. For each of the experiments Torsions II and III use was made of the deformed axial location $z = 110$ mm of the beam's end for both the centerline and the torsion angle which again yield parametric frequencies very close to the excitation frequencies $\omega = 27.0$ Hz for Torsion II and $\omega = 25.5$ Hz for Torsion III that were used in the parametric functions Eq. (5.3). The main difference between the responses of Torsions I–III is that the amplitudes increase as the excitation frequency decreases. In addition, it should be

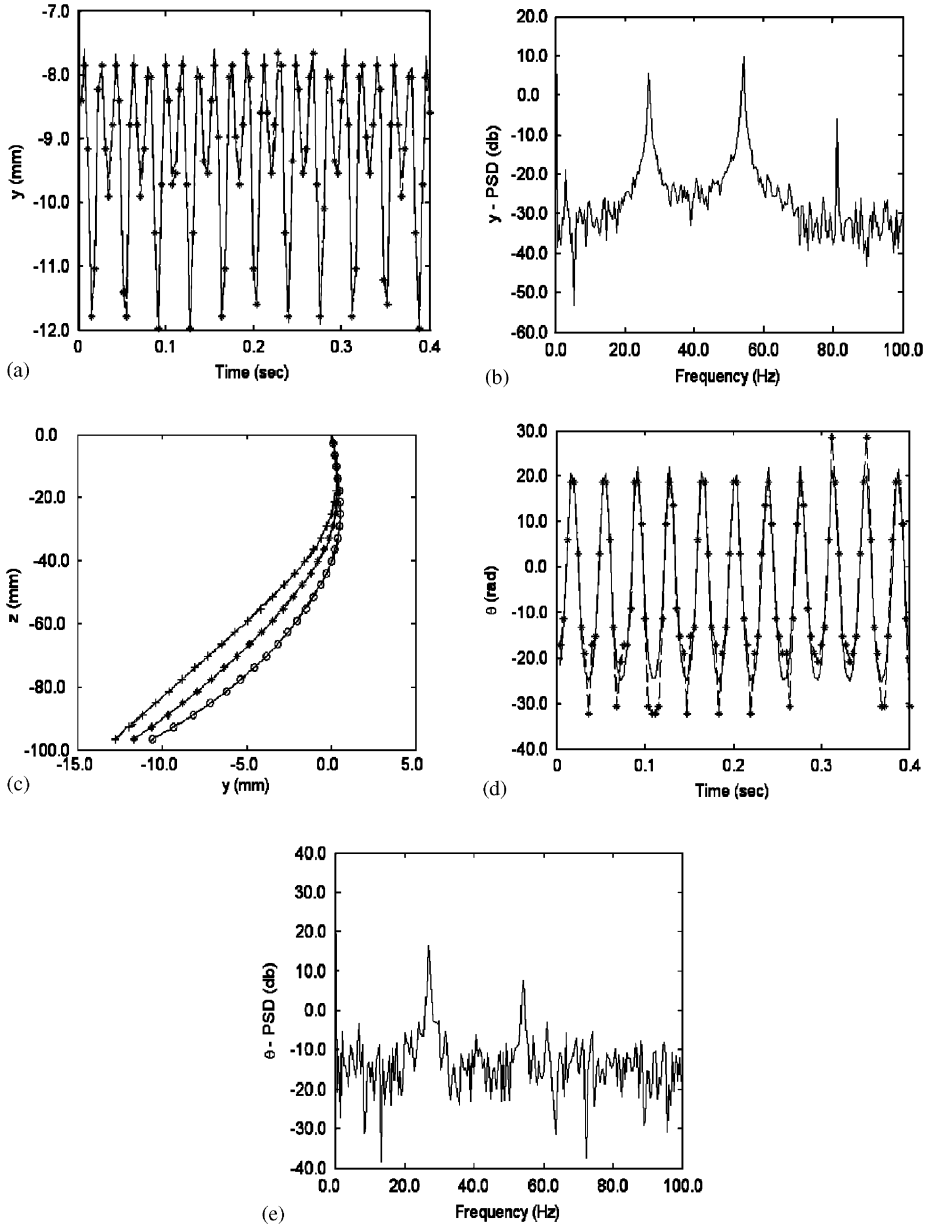

Fig. 12. Response of Torsion II for the centerline (a, b, c) and the torsion angle (d, e). For the time responses (a, b, d, e, with $N = 3$) the deformed axial location is $z = 110$ mm. Also, the spatial shapes (c, with $P = 6$) are presented for different times. The curve labels are: (a, d) (–∗–) Exp.; (—) Par.; (c) (–o–) 0 (ms); (–∗–) 12 (ms); (–+–) 24 (ms).

mentioned that a snap through type bending mode is exhibited near the center of the beam as the torsion angle passes through zero and the stiffness of the beam increases in the stiff bending mode.

Fig. 14 and Tables 10 and 11 analyze the Bending II response using the deformed axial locations $z = 88$ mm and $z = 127$ mm, respectively, for the centerline and the torsion angle. Each of these measurements yields parametric frequencies very close to the excitation frequency $\omega = 35.0$ Hz that was used in the parametric functions Eq. (5.3). From these figures it can be seen that there is very little torsion in this predominantly bending mode. Also, it should be noted that for the response Bending II the axial force in the beam was so large that it caused the extension bar to bend leading to displacements (in the $\mathbf{e}_3$ direction) of about ± 0.5 mm at the beam's clamped end.

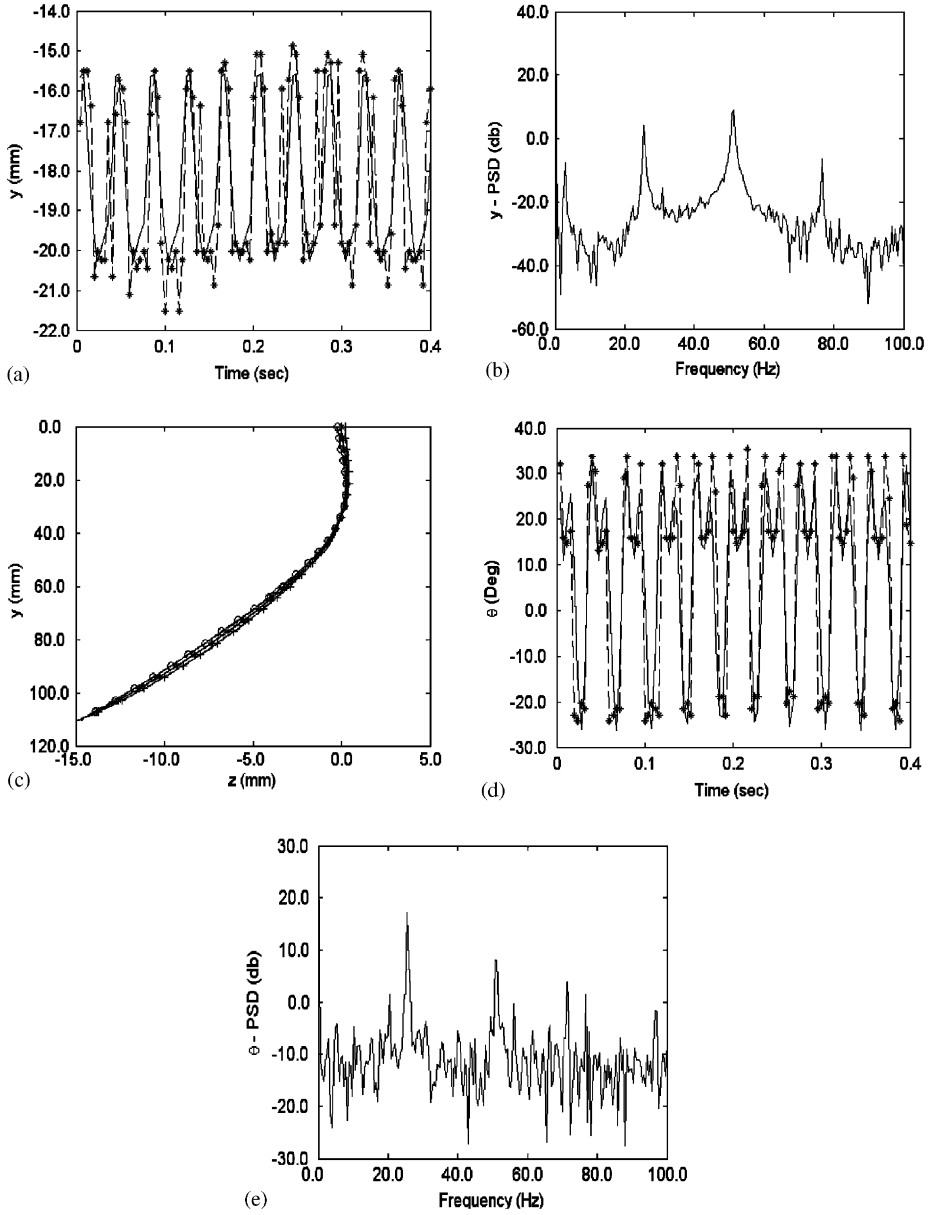

Fig. 13. Response of Torsion III for the centerline (a, b, c) and the torsion angle (d, e). For the time responses (a, b, d, e, with $N = 3$) the deformed axial location is $z = 110$ mm. Also, the spatial shapes (c, with $P = 6$) are presented for different times. The curve labels are: (a, d) (–∗–) Exp.; (—) Par.; (c) (–*o*–) 0 (ms); (–∗–) 13 (ms); (–+–) 18 (ms).

6. Measurement of the natural frequencies and damping

In order to calibrate a finite element model of this beam-mass system it is necessary to first match natural frequencies and damping characteristics. The objective of this section is to provide measurements of these quantities.

The first four natural frequencies and their associated damping coefficients for the orientation of gravity with $\alpha = 1$ were measured by introducing a small perturbation that excited the particular mode of interest. Since the deflections were small, the modes were reasonably uncoupled. Also, the laser sensor was used to measure the associated velocities and the natural frequencies were determined by applying a Fourier transform

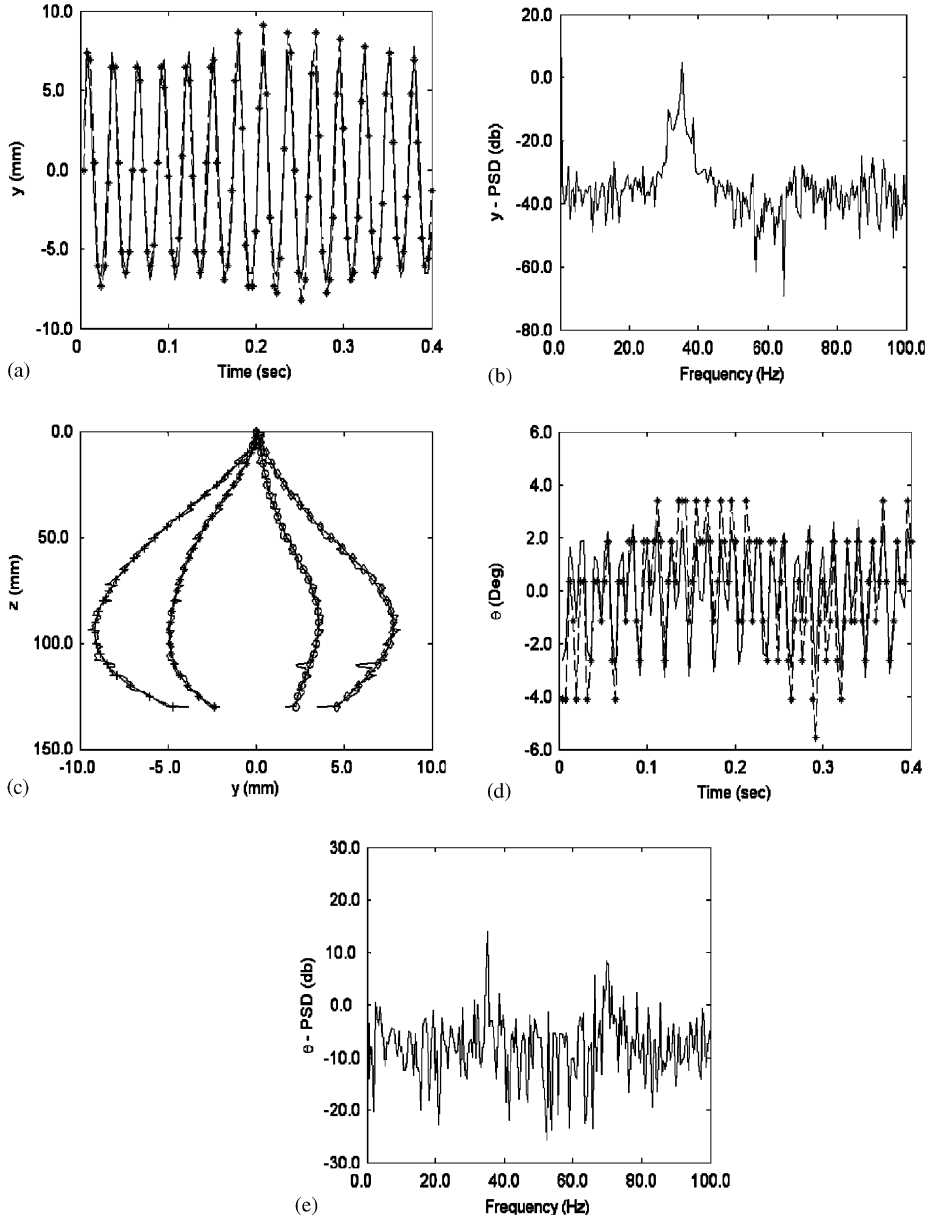

Fig. 14. Response of Bending II for the centerline (a, b, c) and the torsion angle (d, e). For the time responses (a, b, d, e, with $N = 3$) the deformed axial location is $z = 88$ mm for the centerline and $z = 127$ mm for the torsion angle. Also, the spatial shapes (c, with $P = 5$) are presented for different times. The curve labels are: (a, d) (–∗–) Exp.; (—) Par.; (c) (–◇–) 0 (ms); (–o–) 7 (ms); (–∗–) 14 (ms); (–+–) 21 (ms).

to the signal. Fig. 15a shows the velocity and Fig. 15b shows the associated Fourier transform for the first mode in the stiff bending plane. The frequency of this bending mode can easily be determined from the results in Fig. 15b and the damping coefficients for each of the modes were determined using both the time- and frequency-domain methods.

For the time-domain method, the damping was estimated by curve-fitting the decay rate of the envelope (a Hilbert transform was applied to extract the envelop) and the results are shown in Fig. 15c. From linear vibration theory it is known that the envelop in Fig. 15c should have the form

$$v(t) = v_0 \exp(-\zeta\omega t), \tag{7.1}$$

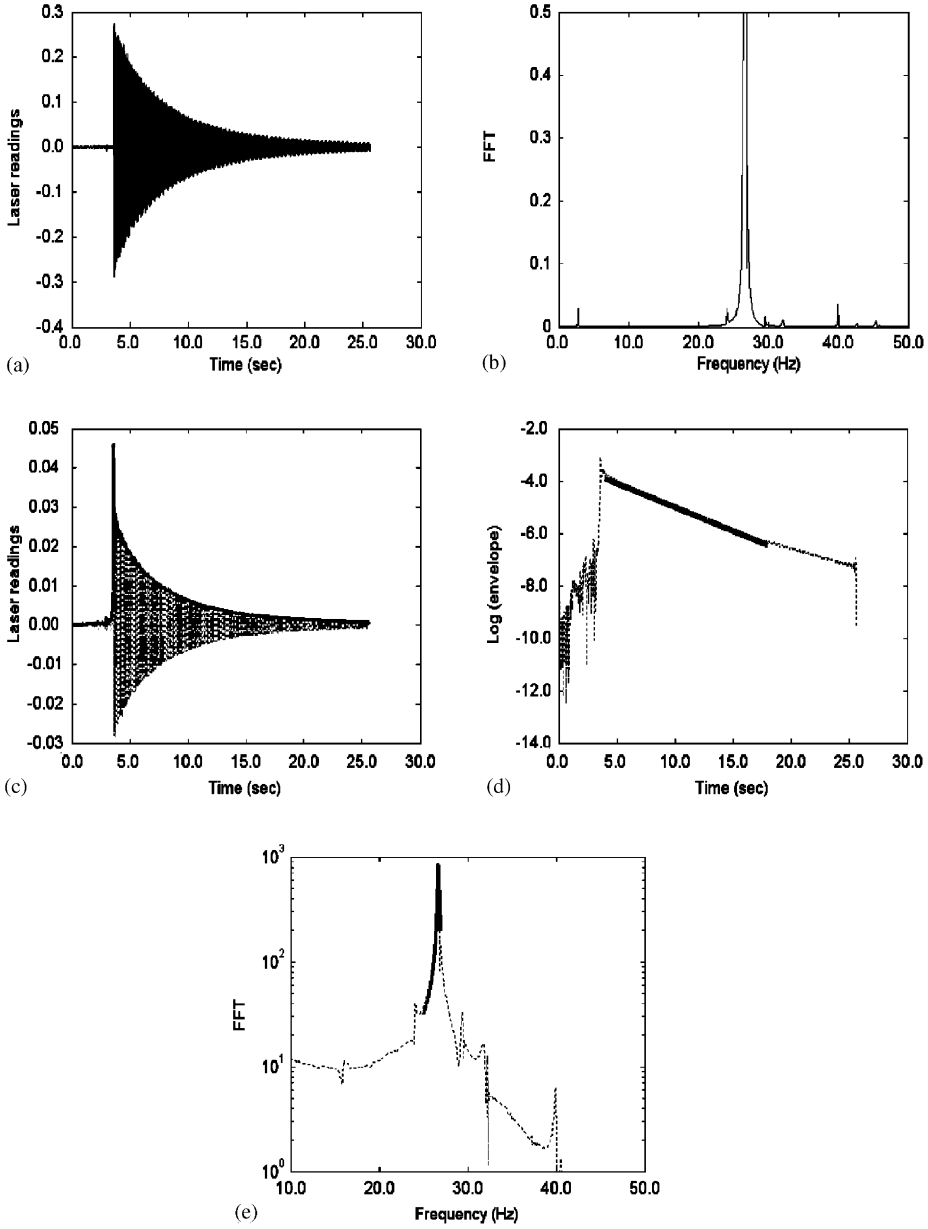

Fig. 15. Analysis of the natural frequency and damping coefficient for the first mode in the stiff bending plane. The curve labels are: (c) (—) Hilbert Transform; (· · · · ·) Measured; (d) (—) Fitted Polynomial; (· · · · ·) Envelope; (e) (· · · · ·) FFT; (—) Fitted.

where ω is the natural frequency and ζ is the normalized damping coefficient. The value of ζ is determined by fitting a straight line to the log plot of this envelope as is shown in Fig. 15d.

For the frequency domain method, a second-order Laplace transform function is fitted to the Fourier transformed signal in a small range of frequencies that contains the desired mode. Fig. 15e shows the results of this process for the range $\omega = 25{-}27$ Hz associated with the first mode in the stiff bending plane. The advantage of this method is that it can be applied to isolate specified modal response even when a number of modes are present. The results of these two methods produced nearly the same answers and the values of the natural frequencies and damping coefficients are recorded in Table 12 for the first four modes of vibration. The values of damping in Table 12 are near the value 0.17% recorded for steel in Ref. [9], except for the value associated with the first bending mode in the weak bending plane which is much higher. This high value of

Table 12
Measured natural frequencies and damping coefficients for the first four modes of vibration ($\alpha = 1$)

Mode type	Frequency (Hz)	ζ (%)
First bending mode (weak plane)	2.76	4.0
First bending mode (stiff plane)	26.75	0.187
Torsional mode	41.82	0.119
Second bending mode (weak plane)	44.03	0.05

damping may be partially due to the flexibility of the extension bar attached to the motor shaft, the damping in the bearings holding this extension bar and effects of the controller.

7. Conclusions

An experimental setup has been designed to investigate dynamic lateral torsional buckling of a beam-mass system. Experiments have been performed and analyzed to present quantitative data in the form of time series of the position of the centerline of the beam and the torsion angle at its end. Measurements have been made using a laser sensor to determine the velocity of points on the mass and also using edge detection of high speed video of the phenomena to determine the motion of the beam. The geometry and material properties of the specimen as well as its natural frequencies and damping coefficients have also been measured.

It has been shown that this dynamic buckling phenomena can occur at different amplitudes and frequencies of excitation (see Torsions I and III in Fig. 6 and the data for Torsion II). Moreover, it has been shown that two different modes of response can occur at the same excitation amplitude and frequency (see Torsion I and Bending II in Fig. 6).

Furthermore, the coefficients of parametric functions of time at different axial locations and polynomial functions of space at different times have been presented for both the position of the beam's centerline and the torsion angle at the beam's end. Such data can be used for future validation of analytical or numerical models.

Acknowledgement

The research of M.B. Rubin was partially supported by his Gerard Swope Chair in Mechanics and by the fund for the promotion of research at the Technion. Also, the authors would like to acknowledge helpful discussions with H. Flashner.

Appendix A. Equations of motion of the beam-mass system

The objective of this appendix is to derive the expressions Eq. (2.4) for the force $\mathbf{f}_L$ and moment $\mathbf{m}_L$ applied to the end $x_3 = L$ of an elastic beam. To this end, let $\mathbf{f}(\mathrm{x}_3)$ and $\mathbf{m}(\mathrm{x}_3)$ be the force and moment applied to the cross-section of the beam at the axial position x_3. Then, the equations of equilibrium of the beam become

$$-\mathbf{f}(0) + \mathbf{f}(\mathrm{x}_3) = 0, \quad -\mathbf{m}(0) + (x_3\mathbf{e}_3 + \mathbf{u}) \times \mathbf{f}(\mathrm{x}_3) + \mathbf{m}(\mathrm{x}_3) = 0, \tag{A.1}$$

where $\{-\mathbf{f}(0), -\mathbf{m}(0)\}$ are the force and moment applied to the beam at its clamped end and $\mathbf{u}$ is the displacement vector. Next, using the boundary conditions

$$\mathbf{f}(L) = \mathbf{f}_L, \quad \mathbf{m}(L) = \mathbf{m}_L, \tag{A.2}$$

it follows from Eq. (A.1) that

$$\mathbf{f}(0) = \mathbf{f}_L, \quad \mathbf{m}(0) = (L\mathbf{e}_3 + \mathbf{u}_L) \times \mathbf{f}_L + \mathbf{m}_L, \tag{A.3}$$

where $\mathbf{u}_L$ is the value of $\mathbf{u}$ at $x_3 = L$. Thus, the equilibrium Eq. (A.1) can be rewritten in the forms

$$\mathbf{f}(x_3) = \mathbf{f}_L, \quad \mathbf{m}(x_3) = \mathbf{m}_L + [(L - x_3)\mathbf{e}_3 + (\mathbf{u}_L - \mathbf{u})] \times \mathbf{f}_L. \tag{A.4}$$

Also, let f_i and m_i denote the components of $\mathbf{f}$ and $\mathbf{m}$, respectively, relative to the fixed base based vectors $\mathbf{e}_i$.

For the problem under consideration the axial component f_3 of the force is assumed to be finite and all other quantities are assumed to be infinitesimal. Thus, Eq. (A.4) yield

$$\begin{aligned} &f_1(x_3) = f_{1L}, \quad f_2(x_3) = f_{2L}, \quad f_3(x_3) = f_{3L},\\ &m_1(x_3) = m_{1L} - (L - x_3)f_{2L} + (u_{2L} - u_2)f_{3L},\\ &m_2(x_3) = m_{2L} + (L - x_3)f_{1L} - (u_{L1} - u_1)f_{3L},\\ &m_3(x_3) = m_{3L}, \end{aligned} \tag{A.5}$$

where quadratic terms in small quantities have been neglected. Moreover, the influence of gravity g can be taken into consideration by specifying f_{3L} in the form

$$f_{3L} = \alpha Mg + EA\frac{u_{3L}}{L}, \quad A = hw, \tag{A.6}$$

where α is an auxiliary parameter introduced for convenience, M is the mass the block attached to the beam's end, and E is Young's modulus of elasticity. Also, here u_{3L} is the displacement from the stretched length caused by gravity. Then, neglecting quadratic terms in the displacements, Eq. (A.5) can be further approximated by

$$\begin{aligned} &f_1(x_3) = f_{1L}, \quad f_2(x_3) = f_{2L}, \quad f_3(x_3) = f_{3L},\\ &m_1(x_3) = m_{1L} - (L - x_3)f_{2L} + (u_{2L} - u_2)\alpha Mg,\\ &m_2(x_3) = m_{2L} + (L - x_3)f_{1L} - (u_{1L} - u_1)\alpha Mg,\\ &m_3(x_3) = m_{3L}. \end{aligned} \tag{A.7}$$

Next, taking into account the finite effect of gravity, the constitutive equations are given by

$$\begin{aligned} &f_3(x_3) = \alpha Mg + EA\frac{\mathrm{d}u_3}{\mathrm{d}x_3},\\ &m_1(x_3) = -EI_{22}\frac{\mathrm{d}^2u_2}{\mathrm{d}x_3^2}, \quad I_{22} = \frac{hw^3}{12},\\ &m_2 = EI_{11}\frac{\mathrm{d}^2u_1}{\mathrm{d}x_3^2}, \quad I_{11} = \frac{h^3w}{12}, \quad m_3 = B_3\frac{\mathrm{d}\theta_3}{\mathrm{d}x_3}, \end{aligned} \tag{A.8}$$

where θ_3 is the torsion angle and the torsional stiffness B_3 is taken from the exact solution [10]

$$\begin{aligned} &B_3 = \frac{\mu h^2b^2}{3}b(\xi), \quad \xi = \frac{b}{h},\\ &b(\xi) = \frac{1}{\xi}\left[1 - \frac{192}{\pi^5\xi}\sum_{n=1}^{\infty}\left[\frac{1}{(2n-1)^5}\right]\tanh\left\{\frac{\pi(2n-1)\xi}{2}\right\}\right] \end{aligned} \tag{A.9}$$

and where μ is the shear modulus

$$\mu = \frac{E}{2(1+\nu)}, \tag{A.10}$$

Next, substituting Eq. (A.7) into Eq. (A.8) and using Eq. (A.6) yields the differential equations

$$\begin{aligned} &EI_{11}\frac{\mathrm{d}^2u_1}{\mathrm{d}x_3^2} - \alpha Mgu_1 = m_{2L} - \alpha Mgu_{1L} + (L - x_3)f_{1L},\\ &EI_{22}\frac{\mathrm{d}^2u_2}{\mathrm{d}x_3^2} - \alpha Mgu_2 = -m_{1L} - \alpha Mgu_{2L} + (L - x_3)f_{2L},\\ &\frac{\mathrm{d}u_3}{\mathrm{d}x_3} = \frac{u_{3L}}{L}, \quad \frac{\mathrm{d}\theta_3}{\mathrm{d}x_3} = \frac{\theta_{3L}}{L}, \end{aligned} \tag{A.11}$$

which are solved subject to the boundary conditions

$$u_1(0)=0,\quad \frac{\mathrm{d}u_1}{\mathrm{d}x_3}(0)=0,\quad u_2(0)=0,\quad \frac{\mathrm{d}u_2}{\mathrm{d}x_3}(0)=0,\quad \theta_3(0)=0. \tag{A.12}$$

Now, introducing the definitions

$$\lambda_1^2=\frac{Mg}{EI_{11}},\quad \lambda_2^2=\frac{Mg}{EI_{22}}, \tag{A.13}$$

the solutions of Eq. (A.11) can be expressed in the forms

For $\alpha=-1$

$$\begin{aligned}
u_1 =& -\frac{1}{Mg}[m_{2L}+Mgu_{1L}+Lf_{1L}]\cos(\lambda_1 x_3)+\left[\frac{f_{1L}}{Mg\lambda_1}\right]\sin(\lambda_1 x_3)\\
&+\frac{1}{Mg}[m_{2L}+Mgu_{1L}+(L-x_3)f_{1L}],\\
u_2 =& -\frac{1}{Mg}[-m_{1L}+Mgu_{2L}+Lf_{2L}]\cos(\lambda_2 x_3)+\left[\frac{f_{2L}}{Mg\lambda_2}\right]\sin(\lambda_2 x_3)\\
&+\frac{1}{Mg}[-m_{1L}+Mgu_{2L}+(L-x_3)f_{2L}],
\end{aligned} \tag{A.14}$$

For $\alpha=0$,

$$\begin{aligned}
u_1 &= \frac{1}{2EI_{11}}[m_{2L}]x_3^2+\frac{1}{6EI_{11}}[(L-x_3)^3-L^3+3L^2x_3]f_{1L},\\
u_2 &= \frac{1}{2EI_{22}}[m_{1L}]x_3^2+\frac{1}{6EI_{22}}[(L-x_3)^3-L^3+3L^2x_3]f_{2L},
\end{aligned} \tag{A.15}$$

For $\alpha=1$,

$$\begin{aligned}
u_1 =& \frac{1}{Mg}[m_{2L}-Mgu_{1L}+Lf_{1L}]\cosh(\lambda_1 x_3)-\left[\frac{f_{1L}}{Mg\lambda 1}\right]\sinh(\lambda_1 x_3)\\
&-\frac{1}{Mg}[m_{2L}-Mgu_{1L}+(L-x_3)f_{1L}],\\
u_2 =& -\frac{1}{Mg}[-m_{1L}-Mgu_{2L}+Lf_{2L}]\cosh(\lambda_2 x_3)-\left[\frac{f_{2L}}{Mg\lambda_2}\right]\sinh(\lambda_2 x_3)\\
&-\frac{1}{Mg}[-m_{1L}-Mgu_{2L}+(L-x_3)f_{2L}],
\end{aligned} \tag{A.16}$$

together with the solutions

$$u_3=\frac{u_{3L}}{L}x_3,\quad \theta_3=\frac{\theta_{3L}}{L}x_3. \tag{A.17}$$

Moreover, the displacements $\{u_{1L}, u_{2L}\}$ and the angles $\{\theta_{1L}, \theta_{2L}\}$ at the end $x_3=L$ are determined by the equations

$$u_{1L}=u_1(L),\quad u_{2L}=u_2(L),\quad \theta_{1L}=-\frac{\mathrm{d}u_2}{\mathrm{d}x_3}(L),\quad \theta_{2L}=\frac{\mathrm{d}u_1}{\mathrm{d}x_3}(L). \tag{A.18}$$

Then, substituting the solutions Eqs. (A.14)–(A.16) into Eq. (A.18) yields equations which can be solved to obtain the expressions Eq. (2.4) where the stiffnesses K_{ij} are given by

For $\alpha = -1$,

$$
\begin{aligned}
K_{11} &= -\frac{Mg\lambda_1}{L\lambda_1 - 2\tan\big((\lambda_1 L)/2\big)},\\
K_{44} &= -\frac{Mg\{\sin(\lambda_1 L) - L\lambda_1\cos(\lambda_1 L)\}}{2\lambda_1\big\{L\lambda_1 - 2\tan\big((\lambda_1 L)/2\big)\big\}\sin\big((\lambda_1 L)/2\big)\cos\big((\lambda_1 L)/2\big)},\\
K_{22} &= -\frac{Mg\lambda_2}{L\lambda_2 - 2\tan\big((\lambda_2 L)/2\big)},\\
K_{33} &= \frac{Mg\{\sin(\lambda_2 L) - L\lambda_2\cos(\lambda_2 L)\}}{2\lambda_2\big\{L\lambda_2 - 2\tan\big((\lambda_2 L)/2\big)\big\}\sin\big((\lambda_2 L)/2\big)\cos\big((\lambda_2 L)/2\big)},\\
K_{14} &= K_{41} = \frac{Mg\tan\big((\lambda_1 L)/2\big)}{L\lambda_1 - 2\tan\big((\lambda_1 L)/2\big)},\\
K_{23} &= K_{32} = -\frac{Mg\tan\big((\lambda_2 L)/2\big)}{L\lambda_2 - 2\tan\big((\lambda_2 L)/2\big)},
\end{aligned}
\tag{A.19}
$$

For $\alpha = 0$,

$$
\begin{aligned}
&K_{11} = \frac{12EI_{11}}{L^3}, \quad K_{44} = \frac{4EI_{11}}{L^2}, \quad K_{22} = \frac{12EI_{22}}{L^3}, \quad K_{33} = \frac{4EI_{22}}{L^2},\\
&K_{14} = K_{41} = -\frac{6EI_{11}}{L^2}, \quad K_{23} = K_{32} = \frac{6EI_{22}}{L^2},
\end{aligned}
\tag{A.20}
$$

For $\alpha = 1$,

$$
\begin{aligned}
K_{11} &= \frac{Mg\lambda_1}{L\lambda_1 - 2\tanh\big((\lambda_1 L)/2\big)},\\
K_{44} &= \frac{Mg\{\sinh(\lambda_1 L) - L\lambda_1\cosh(\lambda_1 L)\}}{2\lambda_1\big\{L\lambda_1 - 2\tanh\big((\lambda_1 L)/2\big)\big\}\sinh\big((\lambda_1 L)/2\big)\cosh\big((\lambda_1 L)/2\big)},\\
K_{22} &= \frac{Mg\lambda_2}{L\lambda_2 - 2\tanh\big((\lambda_2 L)/2\big)},\\
K_{33} &= -\frac{Mg\{\sinh(\lambda_2 L) - L\lambda_2 + \cosh(\lambda_2 L)\}}{2\lambda_2\big\{L\lambda_2 - 2\tanh\big((\lambda_2 L)/2\big)\big\}\sinh\big((\lambda_2 L)/2\big)\cosh\big((\lambda_2 L)/2\big)},\\
K_{14} &= K_{41} = -\frac{Mg\tanh\big((\lambda_1 L)/2\big)}{L\lambda_1 - 2\tanh\big((\lambda_1 L)/2\big)}, \quad K_{23} = K_{32} = \frac{Mg\tanh((\lambda_2 L)/2)}{L\lambda_2 - 2\tanh((\lambda_2 L)/2)}.
\end{aligned}
\tag{A.21}
$$

References

[1] S.P. Timoshenko, J.M. Gere, *Theory of Elastic Stability*, McGraw-Hill, New York, 1961.

[2] J. Dugundji, V. Mukhopadhyay, Lateral bending-torsional vibrations of a thin beam under parametric excitation, *Transactions of the American Society of Mechanical Engineering, Journal of Applied Mechanics* 40 (1973) 693–698.

[3] J.P. Cusumano, F.C. Moon, Chaotic non-planar vibration of the thin elastica, Part I: Experimental observation of planar instability, *Journal of Sound and Vibration* 179 (1992) 185–208.

[4] R.L. Norton, *Machine Design an Integrated Approach*, second ed., Prentice Hall, New Jersey, 1998.

[5] L. Cohen, *Time–Frequency Analysis*, Prentice-Hall, New Jersey, 1995.

[6] D. Gabor, Theory of Communication, *J. IEE (London)* 93 (Part 3) (1946) 429–457.

[7] I. Bucher, O. Wertheim, Measuring spatial vibration using continuous laser scanning, *Shock and Vibration* 7 (2000) 1–6.

[8] S.J. Orfanidis, *Signal Processing*, Prentice Hall, New York, 1996.

[9] H. Kolsky, *Stress Waves in Solids*, Dover, New York, 1963.

[10] I.S. Sokolnikoff, *Mathematical Theory of Elasticity*, McGraw-Hill, New York, 1956.